Geotextiles and Geomembranes 53 (2025) 938–949

Contents lists available at ScienceDirect

Geotextiles and Geomembranes

journal homepage: www.elsevier.com/locate/geotexmem

Regular Paper

Model tests on wicking geosynthetic composite reinforced bases over weak subgrade

Minghao Liu [a], Jiming Liu [a], Sam Bhat [b], Yongxuan Gao [a], Cheng Lin [a,*]

[a] University of Victoria, 3800 Finnerty Road, Victoria, British Columbia, V8P 5C2, Canada
[b] Titan Environmental Containment, 777 Quest Blvd, Ile des Chenes, MB, R0A 0T1, Canada

ARTICLE INFO

Keywords:
Wicking nonwoven geotextile-geogrid composite
Rainfall simulation
Plate loading test
Bearing capacity

ABSTRACT

Road performance is significantly enhanced by incorporating geosynthetics through their reinforcement and drainage functions. This study introduces a novel geosynthetic that integrates these functions. It is made of biaxial polypropylene geogrids heat-bonded to wicking nonwoven geotextiles (WNWGs). WNWGs are chemically treated to be hydrophilic and thus possess rapid wetting and wicking properties while preserving the large lateral drainage functionality of conventional nonwoven geotextiles. To assess the combined reinforcement and drainage performance of this material, a series of model tests including rainfall simulation and plate loading tests were performed on the WNWG-geogrid composite reinforced bases over weak subgrade using a customized model test apparatus. The results confirmed that the inclusion of wicking geosynthetic composite significantly enhanced drainage, stiffness, and bearing capacity of road bases compared to the conventional nonwoven geotextile-geogrid reinforcement and the unreinforced condition. The modulus improvement factor (MIF) for this wicking composite was 2.74 as compared to 1.46 for the conventional nonwoven geotextile-geogrid reinforcement. The findings from this study demonstrate the promising performance of this new composite and provide a valuable reference for full-scale tests and applications on roads.

1. Introduction

Road performance is undermined if water infiltrates the bases and the subgrade and is not adequately drained (Holtz et al., 1998). The detrimental impacts of water include reduced geomaterial strength and stiffness, geomaterial expansion, soil and rock particle erosion, fine particle migration, freeze-thaw damage, asphalt pavement stripping, and durability cracking in concrete (Han, 2015). These pose significant challenges to road maintenance and lead to increasingly economic costs. Therefore, reducing or mitigating the adverse water effect is essential for enhancing the durability and longevity of roads.

Geosynthetics have been successfully used to stabilize soft subgrade and base courses as well as surface courses (Giroud and Han, 2004; Chantachot et al., 2016), effectively extending the lifespan of both unpaved and paved roads. Geotextiles and geogrids are the two primary types of geosynthetics utilized in unpaved road construction (Giroud and Han, 2004). Nonwoven geotextiles are primarily employed for separation, filtration, and drainage, while woven geotextiles serve both separation and reinforcement functions. Geogrids, on the other hand, are typically used for stabilization and reinforcement purposes. As described by Giroud et al. (2021), geosynthetic stabilization/reinforcement is achieved through enhanced load distribution, increased subgrade bearing capacity, and the tensioned membrane effect in roads. Improved load distribution is achieved through the lateral confinement that the geosynthetic provides to the bases (Perkins and Ismeik, 1997), which increases the base course modulus and reduces the maximum load transmitted to the subgrade.

Nonwoven geotextiles have been extensively used for drainage for more than 50 years (Giroud et al., 2021) and have been the subject of numerous studies. Traditional nonwoven geotextiles (NWGs) are effective in laterally draining the water from road bases if they are wetted. However, if wetting is not ensured, the hydrophobic nature of polymers of the NWGs would accumulate water along with the fines at the water-NWG interface (Rollin and Lombard, 1988), resulting in the accumulation of pore water in the bases and thus playing a negative role in roads. Another type of geotextiles, wicking woven geotextiles (WWGs), have been an emerging material used to address the water issue while providing reinforcement to bases (Zhang et al., 2014; Guo et al., 2017, 2019, 2022; Wang et al., 2017; Lin and Zhang, 2018, 2020; Biswas et al., 2021; Lin et al., 2022; Liu et al., 2022; Zaman et al., 2022,

* Corresponding author.
E-mail address: chenglin918@uvic.ca (C. Lin).

https://doi.org/10.1016/j.geotexmem.2025.03.006
Received 2 December 2024; Received in revised form 1 March 2025; Accepted 22 March 2025

2024; Sicha and Zornberg, 2023). As compared to NWGs, WWGs can create spontaneous wetting and wicking through deep-grooved nylon fibers, and thus draw water from bases and the subgrade under both saturated and unsaturated conditions. Several laboratory and field studies have confirmed the effectiveness of wicking geotextile products in removing moisture under both saturated and unsaturated conditions. Zaman et al. (2024) evaluated the moisture reduction ability of WWGs from silty sand and concluded that this geosynthetics can reduce moisture content in silty sand with fines content up to 15 %. Guo et al. (2021) conducted cyclic plate loading test to evaluate the performance of WWG-stabilized aggregated base over subgrade and confirmed that the WWG was able to reduce the water content of base courses effectively in the direction of wicking fibers. However, inheriting from woven geotextiles, WWGs provide less lateral drainage capability as compared to NWGs and less reinforcement as compared to geogrids (Han, 2015).

To overcome the functional limitations of current geosynthetics, this study introduces a wicking geosynthetic composite. This new material is made by biaxial polypropylene geogrids heat-bonded to wicking nonwoven geotextiles (WNWGs), enabling both reinforcement and wicking functions. The WNWGs possess strong wetting and wicking capabilities in addition to the functions that the NWGs have, such as filtration, separation, and drainage (once NWGs are saturated) (Liu et al., 2024; Jarjour and Meguid, 2024). Although this material has been tested at the elemental scale for wicking capability, no research has yet explored its combined reinforcement and wicking functions at the model test level.

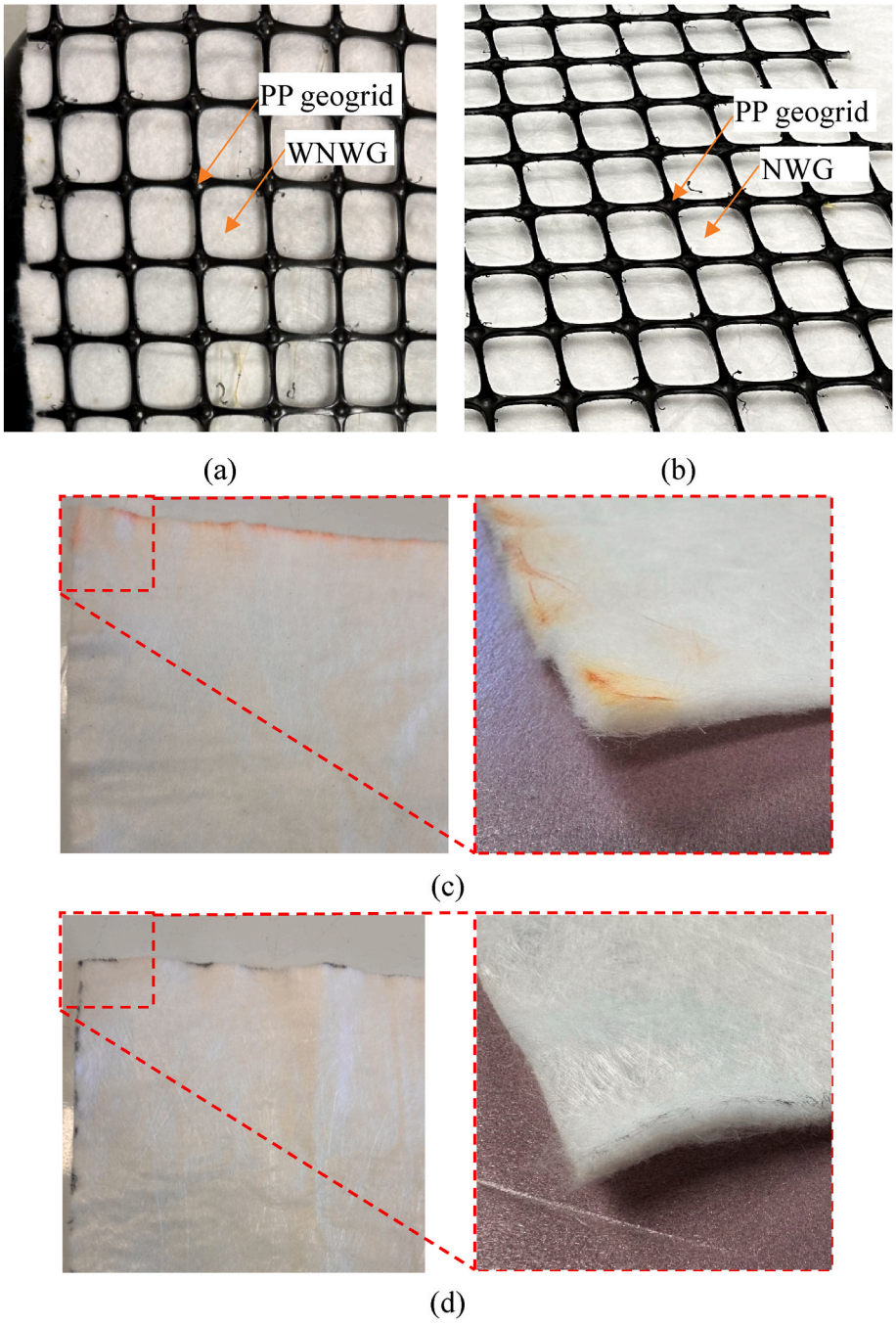

Fig. 1. Geosynthetic materials: (a) the wicking nonwoven geotextile (WNWG)-geogrid composite, (b) nonwicking nonwoven geotextile (NWG) and geogrid, (c) WNWG, and (d) NWG.

The objective of this study was to investigate the efficacy of the proposed wicking geosynthetic composite—i.e., WNWG-geogrid composite—in enhancing the performance of unpaved roads consisting of gravelly bases over the weak soft subgrade. Using a purpose-built model test apparatus, a series of model tests, including precipitation simulation and plate loading, were conducted on three test sections: the WNWG-geogrid composite reinforced bases, the conventional nonwoven geotextile-geogrid reinforced bases, and unreinforced bases. The findings from this study would offer valuable insights into the full-scale tests using this new material and its applications in roads.

2. Materials and methods

2.1. Test materials

The materials used in this study included the proposed wicking geosynthetic composite as well as conventional nonwicking nonwoven geotextile (NWG) and geogrid. The base courses were aggregate, and the subgrade comprised the kaolin-sand mixture.

Fig. 1(a) illustrates the sample of the wicking geosynthetic composite, while Fig. 1(b) depicts the NWG and geogrid samples. The wicking geosynthetic composite, a proprietary product manufactured by Titan Environmental Containment, Ltd., comprises biaxial polypropylene (PP) geogrids heat-bonded to WNWGs. The WNWG is a nonwoven, needle-punched fabric made of continuous polyester (PET) filaments [Fig. 1(c)]. Originally hydrophobic, the PET fibers undergo a chemical treatment that converts the nonpolar C-H functional groups on their surface to polar functional groups (e.g., O-H, COOH, etc.). This treatment enables the fibers to attract polarized water molecules, imparting the hydrophilic properties to WNWG. The WNWG exhibited significant wetting and wicking properties with zero contact angle (highly hydrophilic) and a capillary rise of 30 mm as compared with 140° contact angle (highly hydrophobic) and zero capillary rise for conventional NWG (Liu et al., 2025 under review). Fig. 2 illustrates how the geotextile can remove water from the unpaved road system. For comparison, conventional NWG and biaxial PP geogrid were also tested. The NWG shared the same components and manufacturing process as the WNWG but was not chemically treated [Fig. 1(d)]. The geogrid, a high-stiffness PP biaxial geogrid, was identical to that used in the composite. Table 1 presents the properties of WNWG and NWG, and Table 2 summarizes the properties of the geogrids. In Table 1, the strength parameters (such as grab, punch, and tear strength) for the two geotextile materials are quite similar, suggesting that the chemical treatment did not alter the mechanical properties of the geotextile. In comparison, the strength of the geotextiles was significantly lower than that of the PP geogrid. For instance, the tear strength of the former was less than 1 % of that of the latter.

2.1.1. Base and subgrade materials

This study focuses on the geosynthetic-reinforced unpaved road, and a typical unpaved road section consists of bases layer and the subgrade layer (Giroud et al., 2021). As such, the simulated unpaved road test sections were constructed with an aggregate base layer over the weak subgrade. The subgrade material was a soil mixture consisting of sand and kaolin. The sand was acquired from a local quarry yard in Victoria, Canada, while kaolin was commercial EPK kaolin purchased from Edgar Minerals®. Fig. 3(a) presents the particle size distribution curve for the sand. The subgrade material comprised a mixture of 30 % EPK kaolin and 70 % sand, with the percentages measured in dry mass. It is classified as clayey sand according to the Unified Soil Classification System (USCS). According to Holtz et al. (1998), subgrade stabilization is recommended for weak subgrade with California Bearing Ratios (CBR) below 3 %, while to maximize the geosynthetic functionality of separation and base reinforcement, the CBR values for the subgrade are suggested to range between 3 % and 8 %. Therefore, in this study, the subgrade soil was prepared to a moisture content (13.1 %) corresponding to CBR of 3 %, which was still within 3 % (wet or dry) of the optimum moisture content [11.6 % in Fig. 3(b)], as required in general practice for site preparation.

The base courses were commercial aggregates purchased from Heidelberg Materials®. These aggregates, with a maximum particle size of 25 mm, were classified as well graded base (WGB), a standard material used for pavement base courses in British Columbia, Canada (BC MoTI, 2024). The particle size distribution curve of the aggregates is shown in Fig. 3(a). Fig. 3(b) shows that the aggregate bases had the maximum dry density of 2.11 g/cm^3 and the optimum water content of 6.2 % determined by the Standard Proctor compaction test (ASTM D698, 2021). This test is typically performed as part of a quality control practice for the base courses in British Columbia, Canada (BC MoTI, 2024).

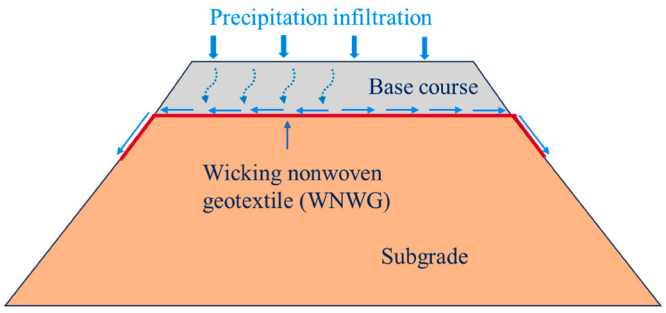

Fig. 2. Conceptual drainage function of WNWG.

Table 1
Properties of wicking and nonwicking nonwoven geotextiles.

Properties	WNWG[a]	NWG**
Apparent opening size, AOS (μm)	194	75
Mass per unit area, M_A (g/m^2)	247	242
Fiber radius, r_f (μm)	8.8	9.8
Permittivity (sec^{-1})	1.82	1.39
Flow rate (L/min/m^2)	5543	4247
Grab strength (N)	962	972
Trapezoidal tear (N)	396	366
CBR puncture strength (N)	2830	3064

[a] WNWG = wicking nonwoven geotextile, with the data provided by Titan and tested by SGI Testing Services, LLC in 2022; **NWG = nonwicking nonwoven geotextile, with the data provided by Titan and tested by SGI Testing Services, LLC in 2024.

Table 2
Properties of geogrids.

Properties	Value	Unit
Radial Stiffness at 0.5 % strain	550	kN/m
Secant Stiffness EA at 0.5 % strain	440	kN/m
Tensile load at 2 % strain	14.39	kN/m
Tensile load at 5 % strain	25.38	kN/m
Ultimate tensile strength	31.5	kN/m
Elongation at break	8.9	%
Junction Efficiency	>95	%
Flexural Rigidity	2,000,000	mg-cm
Aperture Stability	11	Kg-cm/deg
Minimum Rib Thickness	1.5	mm
Aperture Size	34	mm

*Data provided by Titan and tested by SGI Testing Services, LLC in 2024.

2.2. Test setup and instrumentation

In this study, the test section was constructed with a 600 mm thick subgrade layer, a 150 mm thick base course layer, and the wicking geosynthetic composite placed at the subgrade-base interface. To evaluate the efficacy of the composite, another two test sections were

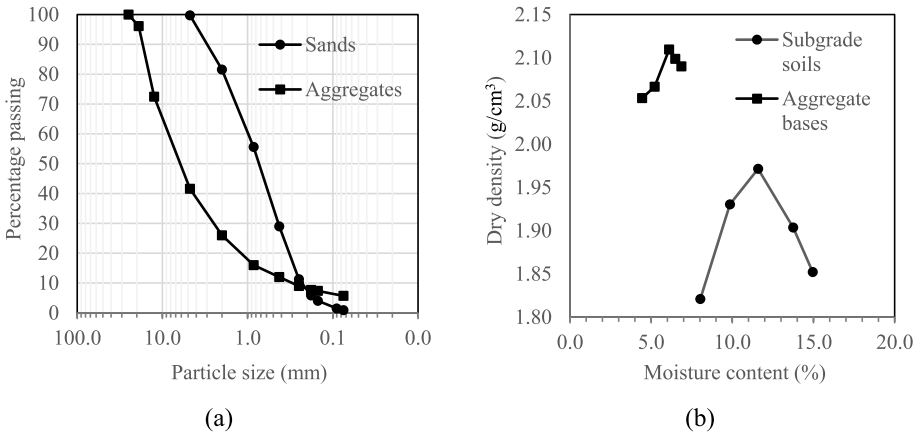

Fig. 3. (a) Particle distribution curves and (b) compaction curve of subgrade and base materials.

considered: a control section without any reinforcement and a comparative section reinforced with NWG and geogrids. All test sections underwent three testing sequences in the purpose-built apparatus (Huang et al., 2021). In this study, the apparatus was upgraded to incorporate rain simulator. Each test sequence started with a rainfall simulation, followed by a drainage period and then a static plate loading test.

2.2.1. Upgrade of model test apparatus

Huang et al. (2021) developed a model test apparatus capable of performing both freeze-thaw tests and plate loading tests, which includes a soil box, a rail connection component, and a plate loading component. This apparatus has been upgraded in this study to incorporate a rain simulator as shown in Fig. 4(a). The freeze-thaw test was not conducted in this study; instead, rain simulation was carried out prior to plate loading tests. The soil box is a square aluminum box with a width of 750 mm. Its height is adjustable as the side walls were constructed with the stacked plates. The details of the soil box were showed in Fig. 4(b). The rail connection component connects the plate loading component to the soil box, allowing soil preparation and rainfall simulation to be performed outside the loading frame. The soil box is moved back to the loading frame through the tracks when plate loading tests are to be performed. A PRO. POINT® 50-ton hydraulic shop press was used to apply static loads. The loading system comprises a hydraulic pump, a hydraulic cylinder, a load cell, and a circular loading plate. The loading plate has a diameter of 150 mm and a thickness of 10 mm. Applied static loads are monitored using a load cell, and the maximum plate load that the system can apply is approximately 109 kN. Static loads are applied manually using the pump handle, with the hydraulic cylinder transferring pressure to the load cell and the loading plate.

According to AASHTO (1993), the minimum compacted base thickness should be at least 100 mm. Therefore, the base course thickness for this study was chosen as 150 mm. For a loading plate with 150 mm in diameter, the minimum depth of soil should be 450 mm per Boussinesq's load distribution. To ensure the depth of soil fully captures the stress influence zone, a subgrade depth of 600 mm was set. This requires the side walls to be 750 mm in height.

A rain simulator was designed and fabricated to be integrated with the soil box for the rain simulation tests, as illustrated in Fig. 4(a). Previous studies on rainfall simulations typically employed rainfall intensities based on maximum values associated with a 5–20 year return period for specific locations, as summarized in Table 3. According to the historical rainfall intensity data provided by the British Columbia Building Code (British Columbia Ministry of Housing, 2024), the maximum recorded 15-min rainfall for a 10-year return period is 18 mm. Based on this data, a rainfall intensity of 1.33 mm/min over a 15-min duration—i.e., 20 mm over 15 min— was adopted in this study to represent an extreme precipitation event in British Columbia, Canada. For the soil box with dimensions of 750 mm × 750 mm, the required flow rate was calculated to be 0.75 L/min for 15 min.

The rainfall simulator comprised ten evenly distributed PVC pipes, each featuring ten equally spaced 1-mm drilled holes. T-shaped or L-shaped adaptors were attached at the ends of the pipes to serve as water inlets. Two wooden stands supported the PVC pipes, securing them in place, as shown in Fig. 5(a). The distance between two adjacent holes or two adjacent pipes was 80 mm, as shown in Fig. 5(b). The water supply portion of the simulator had dimensions of 750 mm × 750 mm like the soil box. Therefore, this rainfall simulator had a mesh with 100 evenly distributed drilled holes that could evenly deliver droplets inside the soil box to simulate natural rainfall. A flow meter [Fig. 5(c)], with a range of 0.2 L/min to 2 L/min, was used to regulate the applied water volume, and the system was connected to a tap water supply. During testing, the rainfall intensity was maintained at 0.75 L/min. The simulator was placed directly on the soil box by positioning the wooden stands above the side walls.

To ensure the uniformity of rainfall distribution at the selected intensity across the test area, a validation test was conducted. Ten collection containers, labeled C1 to C10, were placed beneath the rainfall simulator to capture the discharged water. The test setup is illustrated in Fig. 6. A continuous 10-min water supply was applied, after which the volume of water collected in each container was measured. Since the number of holes covered by each container may vary, the distribution was assessed by calculating the average water output per hole within the covered area of each container. The uniformity of distribution for the rainfall is given by the Christiansen Coefficient of Uniformity (Christiansen, 1942).

$$CU = 1 - \frac{\sum_{i=1}^{n} |X_i - \overline{X}|}{\sum_{i=1}^{n} X_i} \quad (2)$$

where n is the number of holes; X_i is the mass of water outcome from individual hole; $\overline{X}$ is the mean value of mass of water outcome from holes. Given n = 100, $\overline{X} = 77$, the CU of the rainfall simulator is 86 %, which is desirable according to the Irrigation Association (2005). Therefore, the rainfall simulator ensured a uniform distribution of free-falling droplets across the test area.

2.2.2. Soil preparation and instrumentation

The subgrade material was placed and compacted to a CBR of 3 %. Prior to placement, the sand and kaolin were mixed with the calculated water mass, sealed, and left overnight to ensure uniform moisture distribution throughout the soil. The subgrade was compacted in 12 lifts with each being 50 mm thick. A CBR of 3 % for the compacted subgrade

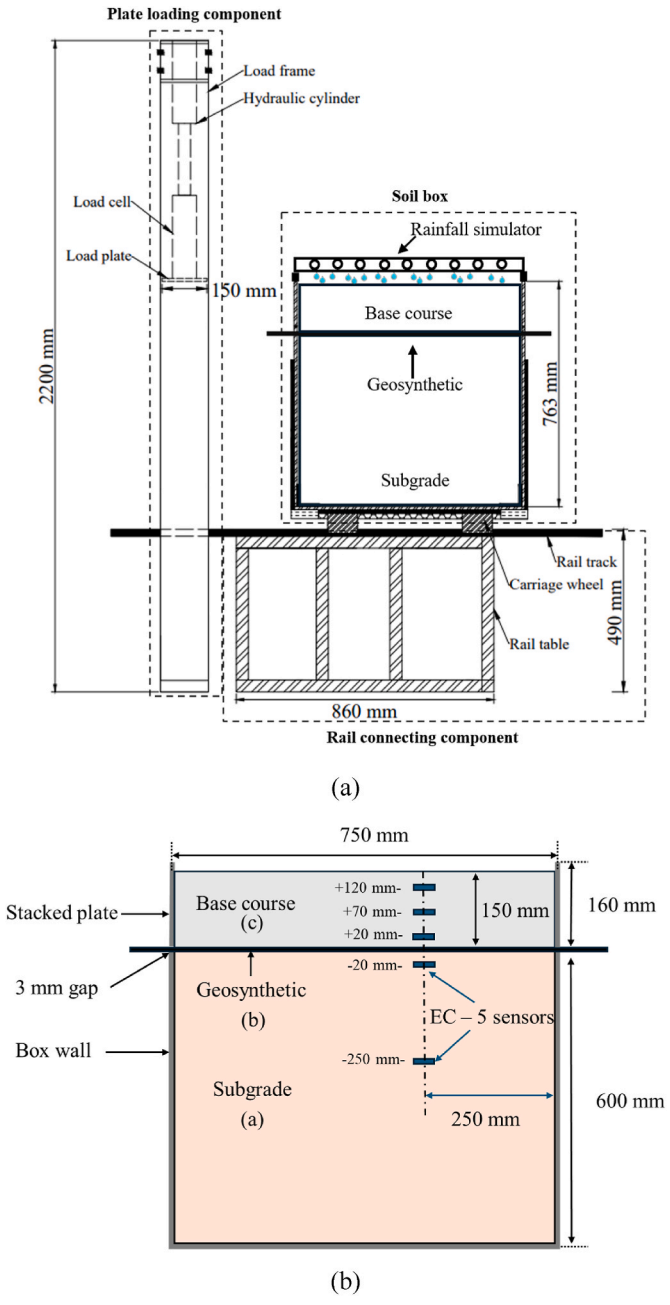

Fig. 4. Schematic of: (a) model test apparatus, and (b) details of soil box.

was achieved by adding the predefined mass of the subgrade material for each lift to ensure the target dry density. A prior test was done to establish CBR values for the compacted curves, which indicated that the target dry density and the corresponding moisture content should be set to 1.93 g/cm^3 and 13.1 %, respectively, to achieve a CBR of 3 %.

After preparing the subgrade [Fig. 7(a)], the wicking geosynthetic composite measuring 750 mm × 1150 mm was added, and the two edges of the composite were extended 200 mm beyond the side walls as shown in Fig. 7(b). For the control section, no geosynthetics were added. For the comparative section, a conventional nonwoven geotextile (NWG) was first added on top of the subgrade overlain by a layer of biaxial geogrid before base courses were added. Both NWG and geogrid were also extended 200 mm beyond the side walls. To enable extending the geosynthetics beyond the side walls, a small gap of 3 mm [(Fig. 4(b)] was created at the side walls at the depth of the subgrade-base interface. Since the gap was slightly smaller than the total thickness of NWG and geogrid, the stacked aluminum plates above the geosynthetics could work as an anchor to prevent NWG and geogrid from slipping against each other during base preparation and plate loading. This same gap was also kept for the control section to ensure the consistency in test conditions.

Table 3
Summary of rainfall simulation setup.

References	Intensity (mm/15 min)	Purpose of rainfall	Criterion	Location
Arnáez et al. (2004)	18.75	Erosion	Not mentioned	Iberian Range, Spain
Egodawatta et al. (2007)	5–33	Road wash	5 years storm event	Gold Coast region, Australia
Navas et al. (1990)	12 & 14.5	Erosion	Maximum 10 years return period	Ebro Valley, Sapin
Sheridan et al. (2008)	25	Road erosion	Not mentioned	Australia
Zemke (2016)	11.25	Soil erosion	Raindrop energy and device limitation	Western Germany
Sosa-Pérez and MacDonald (2017)	11	Soil erosion	20-year period storm	Colorado, US
Guo et al. (2021)	11.4	Drainage behavior	5-year return period precipitation	Douglas County, Kansas

The aggregate bases were compact to 95 % of the degree of compaction at an optimum water content of 6.2 %. Compaction was performed in four lifts, with thicknesses of 20 mm, 50 mm, 50 mm, and 30 mm from bottom to top. The finished surface of the aggregate bases is shown in Fig. 7(c).

Five Decagon EC-5 soil moisture sensors were installed to monitor changes in the volumetric water content in the subgrade and base courses as illustrated in Fig. 4(b). Two EC-5 sensors were placed in the subgrade, respectively, located at 250 mm and 20 mm below the subgrade-base interface. Three sensors were positioned in the base course, respectively, located at 20 mm, 70 mm, and 120 mm above the subgrade-base course interface. These five positions are denoted as −250 mm position, −20 mm position, +20 mm position, +70 mm position, and +120 mm position, respectively. The sensors were positioned along a longitudinal line, 250 mm from the box wall and 125 mm from the center of the box, to minimize the risk of potential damage during the plate loading test.

2.3. Experimental test program

The rainfall simulation was conducted immediately after the preparation of the test sections. The simulation test consisted of 15 min precipitation and several days of drainage. After the precipitation, the surface of the test section was covered with a plastic sheet to limit evaporation from the base course surface. The rain simulation setup is shown in Fig. 8(a). To minimize the impacts of the variations in the ambient temperature and relative humidity, a plastic tent equipped with an air conditioner and humidifier was set up as shown in Fig. 8(b). During the rain simulation tests, the ambient temperature was controlled to 18 °C, and the relative humidity was set to 60 %. The drainage continued until the volumetric moisture content in the base course reached a plateau. After the drainage, plate loading tests were performed.

The circular loading plate, tied to the load cell, was placed on the base course surface and then connected to the piston of the hydraulic cylinder. The hydraulic load cell was connected to the pressure transducer of Omega® XP309 5KG5V and the PASCO® 550 Universal Interface for data readout. The load cell had a capacity of approximately

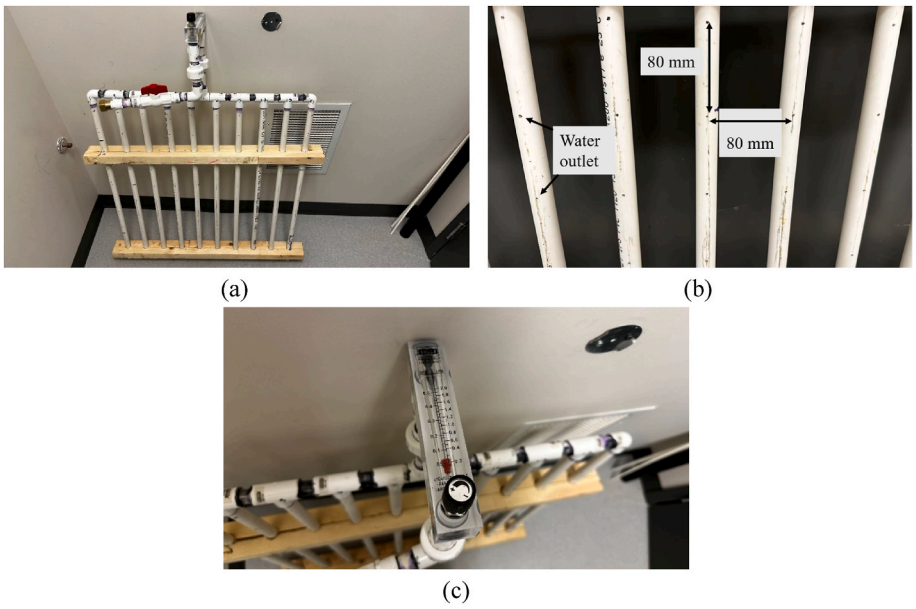

Fig. 5. Photograph of (a) rainfall simulator, (b) details of mesh, and (c) flow meter.

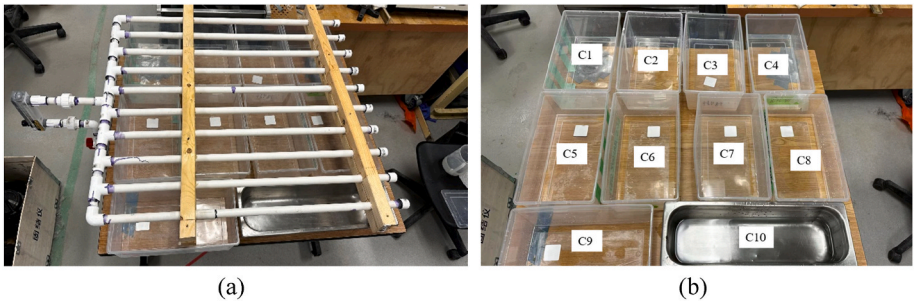

Fig. 6. Rainfall simulator verification test: (a) test setup, and (b) droplet receivers.

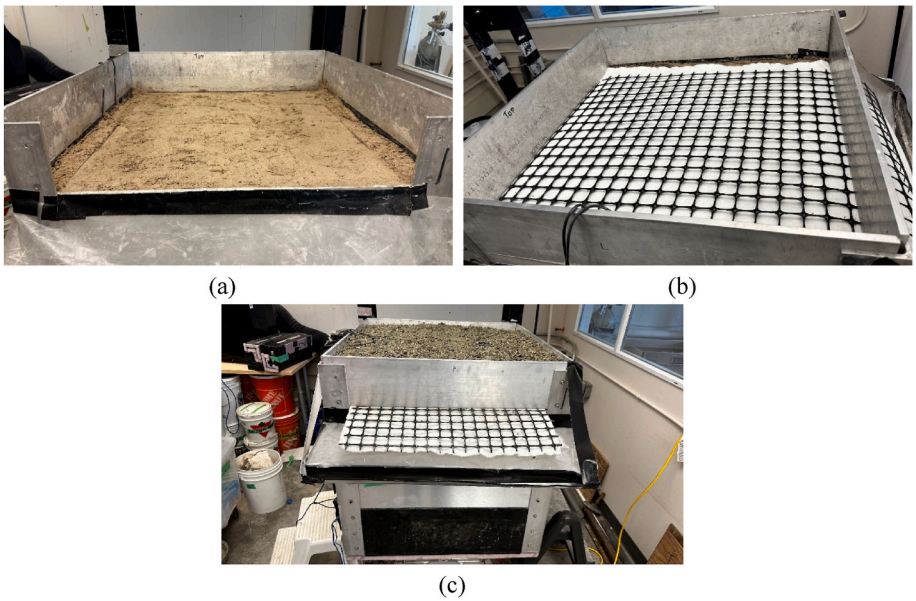

Fig. 7. Setup of the tests: (a) preparation of subgrade, (b) placement of wicking geosynthetic composite, and (c) preparation of base course.

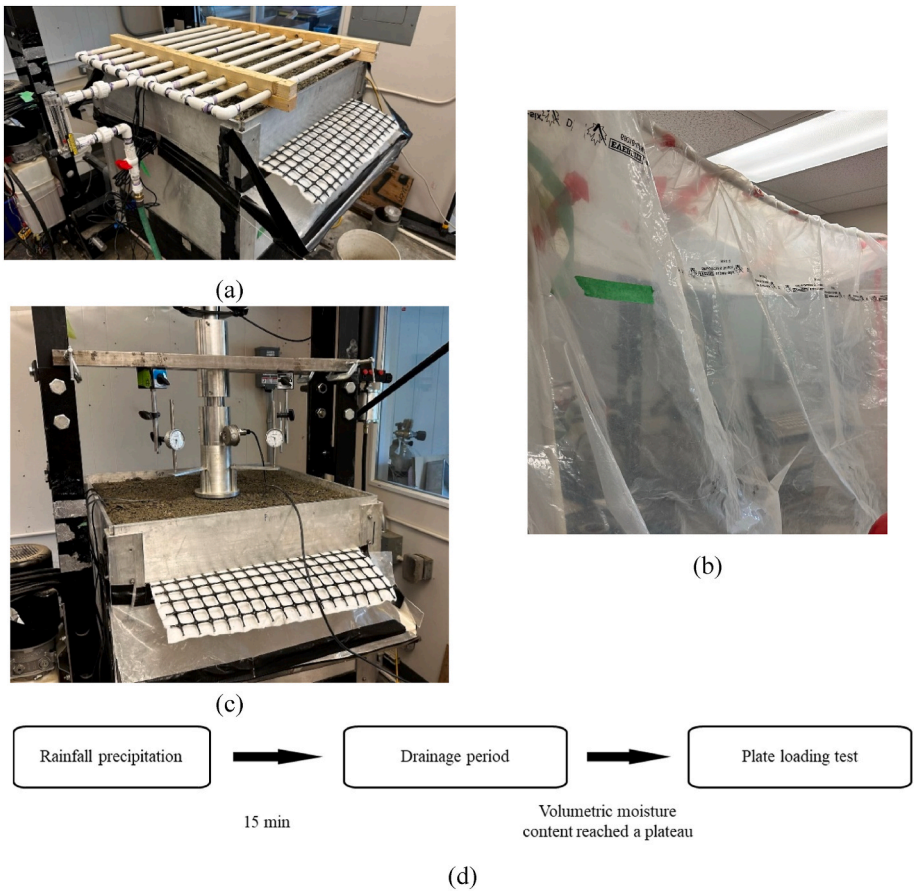

Fig. 8. Operation of rain simulation and plate loading tests: (a) rainfall, (b) drainage covered by plastic tent, (c) plate loading test, and (d) testing procedures.

109 kN, with an accuracy of ±0.25 %. Three dial gauges with a range of 0–50 mm were placed on the three extensions of the loading plate to measure the settlement during the tests. Fig. 8(c) shows a photograph of the plate loading operation. Static loads were applied in increments of 62 or 124 kPa. After the applied load increment caused the settlement to occur at a rapid rate, the load was unloaded to zero. Subsequently, the bases, subgrade, and geosynthetic materials were removed from the box, and the gravimetric moisture content of each material was measured. A flowchart of the testing procedures was shown in Fig. 8(d).

3. Results and discussion

The results of the above-mentioned tests are presented in this section. The wicking efficiency and reinforcement function of the wicking geosynthetic composite (WNWG-geogrid composite) are assessed by comparing them with those from the control section (no reinforcement) and the comparative section (reinforced with conventional geogrids added with a conventional nonwicking nonwoven geotextile).

3.1. Rainfall simulation tests

During the rainfall simulation, water discharge was observed in each test section. In the WNWG-geogrid composite reinforced section, the entire exposed part of the geotextile became partially saturated, with water visibly dripping at the edges of the geotextile. The water-drop procedure continued for 24 h. In the nonwoven geotextile-geogrid reinforced section, no part of the exposed geotextile was saturated, and water tended to flow across the top of the geotextile surface rather than being absorbed or wicked through. The dropping stopped after 30 min after the rainfall terminated. In the control section, without any geosynthetics, water leakage was observed through the gap between the plates.

Fig. 9 present the evolution of volumetric moisture contents over time starting from 15-min precipitation to the end of drainage. The volumetric moisture content θ was measure directly by the EC-5 soil moisture sensors, given by Equation (2):

$$\theta = \left(8.5{*}10^{-4}\right)(RAW) - 0.48 \quad (2)$$

where RAW is the output from the data logger using 3-V excitation.

To better present the changes in the volumetric moisture content, the measured values at given times are subtracted from the initial values, as presented in the time history of variations of volumetric moisture content in Fig. 9(a), (d), and 9(g). For clearer observation,Fig. 9(b), (e), and 98(h) show the evolution for the first 30 h. However, the measured values are presented in the volumetric moisture content profiles in Fig. 9 (e), (f), and 9(i) at the designated time: at the start of precipitation (SOP), at the end of precipitation (EOP), 30 min after precipitation, 1 day after precipitation, 7 days after precipitation, and 21 days after precipitation. The zero position (i.e., 0 mm) refers to the location of the geosynthetics for the reinforced sections or the base course-subgrade interface for the control section.

Fig. 9(a) shows that for the WNWG-geogrid composite reinforced section, the volumetric moisture contents in the base courses—i.e., at positions of +120 mm, +70 mm, +20 mm—dropped rapidly after precipitation. Subsequently, they gradually decreased and stabilized on the 21st day. After 21 days, the volumetric moisture content also reached a plateau in the subgrade. Compared to the initial volumetric moisture content, which was measured immediately before precipitation, the volumetric moisture content at the +20 mm position exhibited the most significant reduction by 5.5 %. The volumetric moisture content at the +70 mm position also decreased, although to a lesser extent by 4.6 %.

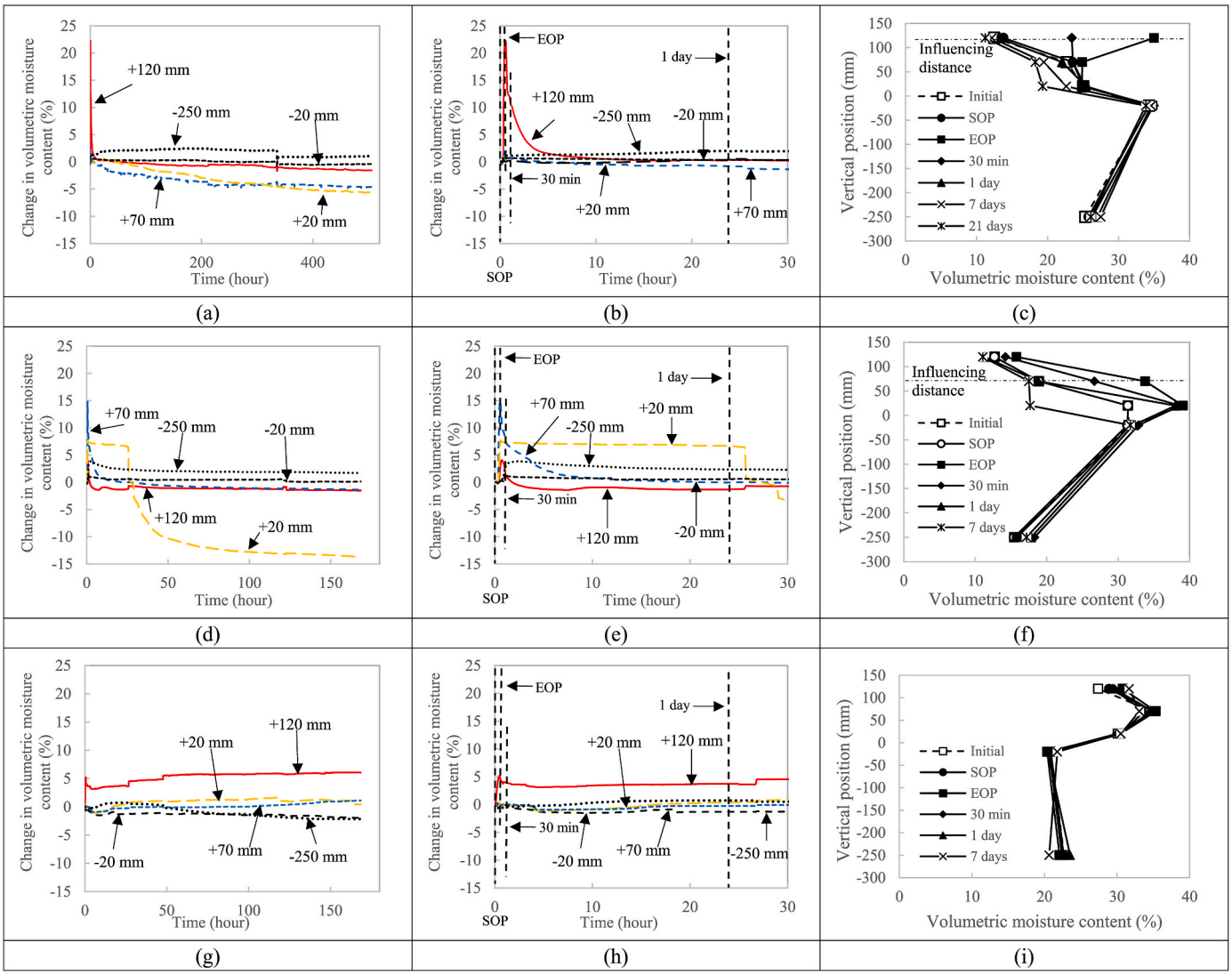

Fig. 9. Rainfall simulation results: (a), (b), and (c) time history of changes in volumetric moisture content in the section with WNWG-geogrid composite; (d), (e) and (f) time history of changes in volumetric moisture content in the section with NWG& geogrid; (g), (h) and (f) time history of changes in volumetric moisture content in the section without reinforcement.

On the other hand, the volumetric moisture content at the +120 mm position showed the least change, and it eventually returned to its initial level. As opposed to the base courses, the subgrade experienced negligible changes in the volumetric moisture content during the entire testing duration.

Kissa (1996) defined wetting as a process of replacing the fiber-air interface with the fiber-water interface and wicking as a process to move the water in a porous substrate. Both can be driven by spontaneous forces such as capillary or external forces such as gravity or external load. WNWG is capable of conducting both functions. Its hydrophilic properties of modified fibers can create capillary action while its inherent properties of high permittivity and transmissivity (in-plane flow rate) (Table 1) from the conventional NWG allow for lateral water movement driven water head difference. Results shown in Fig. 9 confirm that the WNWG possessed spontaneous and forced wetting and wicking capabilities. At a higher position such as +120 mm, the forced wetting and wicking dominated as the flow was driven by the water head difference—i.e., gravity, while at a lower position such as +20 mm, the spontaneous wetting and wicking dictated. The former was evidenced by the volumetric moisture content returning to the initial level while the latter was manifested by the decrease in volumetric moisture content as compared to the initial. Since the final value at +70 mm was 4.5 % lower than the initial value, while at +120 mm, the final value was 0.8 % lower than the initial value, it is suggested that the influencing vertical distance of the spontaneous wicking was close to +120 mm in the aggregate bases as shown in Fig. 9(a). Both wetting and wicking are anticipated to involve vertical (perpendicular to plane) and lateral (in-plane) movement of water. In general, lateral movement was dominant as water came out from the exposed edges of the WNWG during the rainfall test while the volumetric moisture content in soils immediately below the WNWG remained unchanged [Fig. 9(c)].

In the comparative section [Fig. 9(d) and (e)], the volumetric moisture content at the +120 mm position also showed a rapid drop with the final values returning to the initial level, while that at the +70 mm position also exhibited a quick decrease, which however took a longer duration to return the initial level. In contrast, the volumetric moisture content at the +20 mm position exhibited a distinct response. After the precipitation, the volumetric moisture content maintained at the peak values for approximately 25 h before plummeting. After 7 days, the volumetric moisture content reached a plateau. This result indicated the conventional nonwoven geotextile did not possess the spontaneous wetting and wicking capability; instead, it created a barrier for the water flow if the water head at the position was low such as the +20 mm position. After 25 h, the geotextile reached a breakthrough of flow under

the water head up to 150 mm, resulting in the occurrence of wetting and following lateral drainage. This progress allowed the NWG to drain water from the aggregate bases at a +20 mm position through hydraulic gradient, then reduced the volumetric moisture content by 13 % compared to its initial value after 7 days. Fig. 9(d) indicates that the water accumulation was more concentrated at +20 mm and +70 mm positions right after precipitation, which was in contrast to the water accumulation at +120 mm position in the WNWG-geogrid composite reinforced section as shown in Fig. 9(a). This also confirmed the spontaneous wetting and wicking capability of WNWGs.

In the control section, as shown in Fig. 9(g),(h), and Fig. 9(i), the volumetric moisture content at +120 mm increased immediately to the peak during the precipitation, which then maintained at the peak for the rest of the week. All other layers showed minimal change, remaining stable throughout the entire period. This behavior represents the water accumulation observed when there were no geosynthetics present to perform a drainage function.

The measurement of volumetric moisture content in geotextiles was not feasible with current instrumentation. Consequently, the gravimetric moisture content of geotextiles was determined by oven drying the cut piece of geotextiles after all the tests were completed, including the plate loading tests. The geotextiles were retrieved, cut into 150 mm wide and 750 mm long strips with the cutting direction aligned with the front edge of the aluminum box, and then oven-dried. Fig. 10 illustrates the gravimetric moisture content distribution along the length of the geotextiles, and the average gravimetric moisture contents of geotextiles were shown in Table 4. It is interesting that NWG specimens exhibited significantly higher gravimetric moisture content than WNWG specimens, while the exposed edges remained dry in both types of geotextiles. Furthermore, in the comparative section, the central areas of the NWG—i.e., distance of 160–600 mm from the left side wall—maintained a relatively higher gravimetric moisture content compared to the edges of the NWG. This indicated that water was retained within the NWG and was not effectively drained out. In the WNWG-geogrid composite reinforced section, most of the water from the base courses was effectively transported out of the WNWG, as evidenced by low uniformly distributed gravimetric moisture content along the length of WNWG. Both spontaneous and forced wetting and wicking enabled the WNWG to facilitate continuous wicking and lateral water transport. In contrast, once forced wetting ceased, NWG specimens could not drain or transport water effectively, leading to moisture accumulation within the geotextile layer.

It is worth noting that during the compaction process of the base courses, water started to be drained out in the WNWG-geogrid composite reinforced section. Therefore, the initial value of the volumetric moisture content of the base courses in this section was lower than the designed value. Thus, a direct comparison of the measured values of the volumetric moisture content between different sections might not be proper; however, examining the relative differences in volumetric moisture content is meaningful and adequate for the comparison.

Table 4
Gravimetric moisture content of aggregate and geotextile after loading.

Test section	Gravimetric moisture content (%)			
	Aggregates			Geotextiles
	+120 mm position	+70 mm position	+20 mm position	
Wicking geosynthetic composite (WNWG-geogrid composite)	3.72	3.97	4.67	29
Comparative (NWG& geogrid)	3.89	4.13	4.26	212
Control (no reinforcement)	6.75	7.19	7.13	–

3.2. Plate loading tests

Plate loading tests were performed for each section following the rainfall simulation, and the results are presented in Fig. 11. The initial steep slopes under small load, which were caused by sitting errors due to the surface irregularities and incomplete contact between soil and loading plate, were corrected by linearly extending the middle linear portion. The stiffness of soils, k, is defined as the initial slope of the corrected curve. When the plunging load is not discernible, as revealed in Fig. 11, the ultimate bearing pressure, p_u, was determined as the applied pressure having the maximum curvature (Adams and Collin, 1997; Rajagopal et al., 2014). The improvement factor, defined as the ratio of bearing capacity or stiffness between reinforced and unreinforced base course, was used to quantify the benefit of geosynthetics (Pokharel et al., 2010). The results of bearing capacity, stiffness, and improvement factor were investigated based on corrected pressure-displacement curves and summarized in Table 5. The gravimetric moisture content of base course at different depth were measured and shown in Table 4.

Fig. 11 demonstrates that the WNWG-geogrid composite reinforced section was strongest with the load-displacement curve located above the other two curves. The nonwoven geotextile-geogrid reinforced section also showed a stiffer response than the unreinforced section. In general, both reinforced sections exhibited an improvement in performance after rainfall simulation. Table 5 presents the quantitative improvements in terms of bearing capacity and stiffness. The bearing capacity in the comparative section was 16 % higher than the control

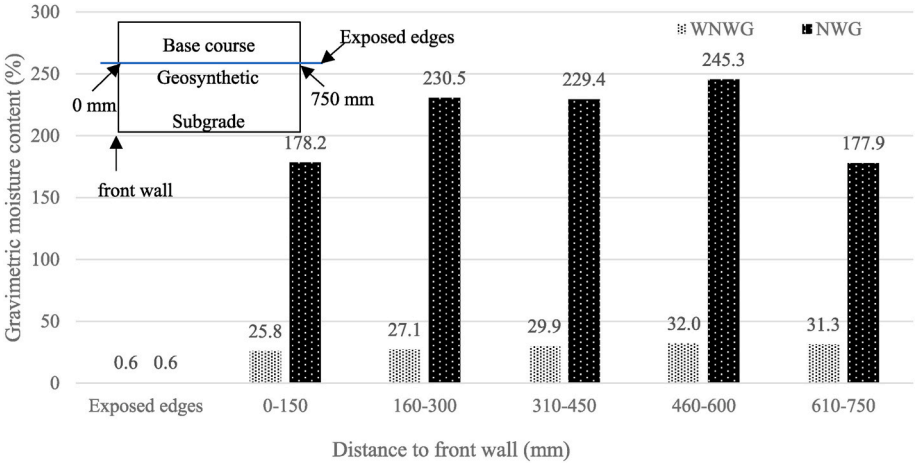

Fig. 10. Moisture content distribution of geotextiles.

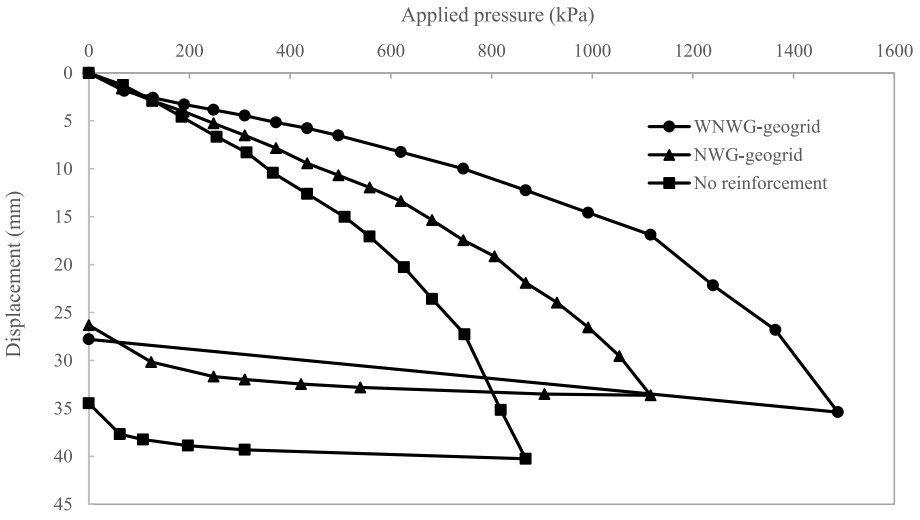

Fig. 11. Plate loading test results for different sections.

Table 5
Bearing capacity and stiffness with different geosynthetics.

Test section	Bearing capacity (kPa)	Improvement factor	Stiffness (kPa/mm)	Improvement factor
Wicking geosynthetic composite (WNWG-geogrid composite)	1178	1.58	96	2.74
Comparative (NWG& geogrid)	868	1.16	51	1.46
Control (no reinforcement)	746	–	35	–

section, while the WNWG-geogrid composite reinforced section had 58 % higher bearing capacity. This indicates that the wicking geosynthetic composite provided an additional 42 % improvement compared to the reinforcement with conventional nonwoven geotextiles and geogrids. Moreover, the reinforced test sections exhibited a more significant increase in stiffness. The stiffness was enhanced by 46 % with the conventional NWG and geogrid reinforcement, compared to the control section, and by 174 % with the wicking geosynthetic composite reinforcement. The modulus improvement factor (MIF) for geosynthetic reinforced bases typically ranges between 1.0 and 2.0 (Han, 2015). The improvement factor for stiffness for the nonwoven geotextile-geogrid reinforced section fell in this range. However, that for the WNWG-geogrid composite reinforced section exceeded this range, demonstrating substantial improvement. It is worth noting that the geogrid components of the geosynthetic reinforcement in both reinforced test sections are identical. Therefore, the improvements in bearing capacity and stiffness observed above were solely attributed to the strong wetting and wicking behavior of WNWG.

For soils with constant dry density, drying from the optimum moisture content leads to an increase in the CBR value and higher matric suction (Ampadu, 2007). Both CBR and matric suction exhibit a positive correlation with the resilient modulus (Lim et al., 2022). Costa et al. (2003) conducted static plate loading tests on unsaturated lateritic soil

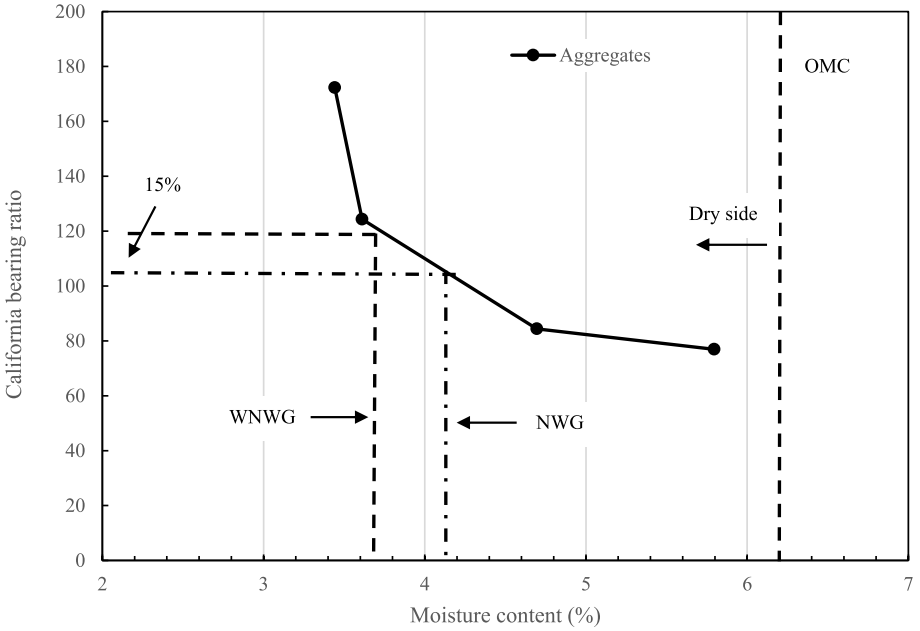

Fig. 12. Variation of CBR with moisture content for aggregates.

and concluded that an increase in soil matric suction results in enhanced bearing capacity. To verify the CBR variation in the aggregate base in this study, a series of CBR test for the aggregates, with the gravimetric moisture content ranging from the gravimetric water content of aggregate bases after plate loading test (3.7 %) to its optimum moisture content (OMC) (6.2 %), were conducted. The variation of CBR value were shown in Fig. 12. The results showed that as the soil dried from the OMC, the CBR increased and the increase became more rapidly as the moisture content reduced further. The results of the present study are in agreement with Ampadu (2007). The improvement in CBR values of aggregates at +120 mm and +70 mm positions due to moisture reduction caused by WNWG was approximately 15 %. This confirmed the higher stiffness and bearing capacity of the base courses due to water reduction by inclusion of WNGW as compared with NGW.

Moreover, as noted previously, the NWG specimens exhibited significantly higher moisture content than WNWG specimens after the plate loading tests. Therefore, the soil-geotextile interface suction in these two sections were affected by the moisture content differences. The moisture content difference between aggregates (+20 mm position) and WNWG-geogrid composite and that between aggregates and NWG & geogrid reinforced sections were 24 % and 207 %, respectively, as shown in Table 5. Therefore, the matric suction at the interface of NWG and aggregates, was much lower than that of WNWG and aggregates. Khoury et al. (2011) conducted suction-controlled direct shear tests to investigate the soil-geotextile interface shearing behavior in unsaturated soil conditions. Their results shown that for given suctions with an equilibrium moisture contents, the increased suction at the interface lead to increase of peak shear strength of soil-geotextile interface and an increase in the interface adhesion. Therefore, in this study, with higher moisture content, the unsaturated soil-geotextile interface of NWG and geogrid reinforcement processes lower shear strength than that of WNWG-geogrid composite reinforcement, which lead to lower bearing capacity.

The findings from this study highlight the promising wicking potential and reinforcement capabilities of the WNWG-geogrid composite, which can be useful for its application in both unpaved and paved roads. The results suggest that the WNWG-geogrid composite could offer superior performance in water management, particularly in road construction, by integrating the functionalities of conventional nonwoven geotextiles and geogrids, along with strong wetting and wicking capability. This composite is especially advantageous for roads in regions experiencing heavy precipitation and freeze-thaw cycles, where efficient drainage is crucial for maintaining road stability. As a first design approximation, the modulus improvement factor (MIF) of 2.74 obtained from this study may be used when designing it with AASHTO (1993) as currently there is no design available for this new material in roads. Furthermore, the outcomes of this study provide an important reference for future research on WNWG-geogrid composites in the field scale, ultimately contributing to the development of appropriate design method.

4. Conclusions

This study introduces a novel wicking geosynthetic composite, comprised of wicking nonwoven geotextile (WNWG)-geogrid composite. Through a series of model tests consisting of rainfall simulation tests followed by plate loading tests, the following conclusions are drawn:

- The control (unreinforced) test section experienced increased water accumulation and reduced bearing capacity and stiffness, highlighting the importance of incorporating both wicking and reinforcement functions to improve road performance.
- WNWG possessed significant wetting and wicking capability, rapidly reducing water in the base courses immediately after heavy precipitation. In contrast, the conventional nonwicking nonwoven geotextile (NWG) created a barrier at soil-geosynthetic interface preventing water flow, leading to temporary water accumulation above the geotextile.
- The WNWG-geogrid composite significantly improved the stiffness and bearing capacity of the test section as compared to the conventional geosynthetic reinforcement (NWG and geogrid) and no reinforcement. The modulus improvement factor for the WNWG-geogrid composite reinforced section was 2.74 as compared to 1.46 for NWG-geogrid reinforced section.
- Both rainfall simulation and plate loading tests confirmed the pronounced wicking and reinforcement functions of the proposed WNWG-geogrid composite in this study.

CRediT authorship contribution statement

Minghao Liu: Writing – original draft, Validation, Methodology, Investigation, Formal analysis, Data curation. **Jiming Liu:** Methodology, Investigation, Formal analysis. **Sam Bhat:** Writing – review & editing, Supervision, Funding acquisition. **Yongxuan Gao:** Investigation, Data curation. **Cheng Lin:** Writing – review & editing, Validation, Supervision, Project administration, Methodology, Investigation, Funding acquisition, Conceptualization.

Acknowledgements

This research is financially supported by the Natural Sciences and Engineering Research Council (NSERC) (ALLRP 581402-23), MITACS (IT35660), and Titan Environmental Containment, Ltd. through the Alliance-Accelerate Joint Program. The authors are grateful for their support. Mr. Bastien Lanusse and Mr. Solomon Rosenberg from the Department of Civil Engineering at the University of Victoria have assisted in apparatus modification. Their assistance in this study is greatly appreciated.

Data availability

Data will be made available on request.

References

Adams, M.T., Collin, J.G., 1997. Large model spread footing load tests on geosynthetic reinforced soil foundations. J. Geotech. Geoenviron. Eng. 123 (1), 66–72. https://doi.org/10.1061/(ASCE)1090-0241(1997)123:1(66.

American Association of State Highway and Transportation Officials, 1993. Guide for Design of Pavement Structures. AASHTO.

Ampadu, S.I.K., 2007. A laboratory investigation into the effect of water content on the CBR of a subgrade soil. Experimental unsaturated soil mechanics 112, 101–110. Springer.

Arnáez, J., Larrea, V., Ortigosa, L., 2004. Surface runoff and soil erosion on unpaved forest roads from rainfall simulation tests in northeastern Spain. Catena 57 (1), 1–14. https://doi.org/10.1016/j.catena.2003.09.002.

ASTM D698, 2021. Standard Test Methods for Laboratory Compaction Characteristics of Soil Using Standard Effort, vol. 12, p. 400 ft-lbf/ft3 (600 kN-m/m3)).

Biswas, N., Puppala, A.J., Khan, M.A., Congress, S.S.C., Banerjee, A., Chakraborty, S., 2021. Evaluating the performance of wicking geotextile in providing drainage for flexible pavements built over expansive soils. Transp. Res. Rec.: J. Transport. Res. Board 2675 (9), 208–221. https://doi.org/10.1177/03611981211001381.

British Columbia Ministry of Housing, 2024. British Columbia building code. https://www.bccodes.ca/.

British Columbia Ministry of Transportation and Infrastructure, 2024. Standard Specifications for Highway Construction, vols. 1 & 2. https://www2.gov.bc.ca/gov/content/transportation/transportation-infrastructure/engineering-standards-guidelines/standard-specifications-for-highway-construction.

Chantachot, T., Kongkitkul, W., Youwai, S., Jongpradist, P., 2016. Behaviours of geosynthetic-reinforced asphalt pavements investigated by laboratory physical model tests on a pavement structure. Transportation Geotechnics 8, 103–118. https://doi.org/10.1016/j.trgeo.2016.03.004.

Christiansen, J.E., 1942. Irrigation by Sprinkling, vol. 4. Berkeley, California: Agricultural Experiment Station.

Costa, Y., Cintra, J., Zornberg, J., 2003. Influence of matric suction on the results of plate load tests performed on a lateritic soil deposit. Geotech. Test. J. 26 (2), 219–227. ASTM International.

Egodawatta, P., Thomas, E., Goonetilleke, A., 2007. Mathematical interpretation of pollutant wash-off from urban road surfaces using simulated rainfall. Water Res. 41 (13), 3025–3031. https://doi.org/10.1016/j.watres.2007.03.037.

Giroud, J.P., Han, J., 2004. Design method for geogrid-reinforced unpaved roads. I. Development of design method. J. Geotech. Geoenviron. Eng. 130 (8), 775–786. https://doi.org/10.1061/(ASCE)1090-0241(2004)130:8(775.

Giroud, J.P., Han, J., Tutumluer, E., Dobie, M.J.D., 2021. The use of geosynthetics in roads. Geosynth. Int. 30 (1), 47–80. https://doi.org/10.1680/jgein.21.00046.

Guo, J., Han, J., Zhang, X., Li, Z., 2019. Evaluation of moisture reduction in aggregate base by wicking geotextile using soil column tests. Geotext. Geomembranes 47 (3), 306–314. https://doi.org/10.1016/j.geotexmem.2019.01.014.

Guo, J., Han, J., Zhang, X., Li, Z., 2021. Experimental evaluation of wicking geotextile-stabilized aggregate bases over subgrade under rainfall simulation and cyclic loading. Geotext. Geomembranes 49 (6), 1550–1564. https://doi.org/10.1016/j.geotexmem.2021.07.004.

Guo, J., Wang, F., Zhang, X., Han, J., 2017. Quantifying water removal rate of a wicking geotextile under controlled temperature and relative humidity. J. Mater. Civ. Eng. 29 (1), 04016181. https://doi.org/10.1061/(ASCE)MT.1943-5533.0001703.

Guo, Y., Lin, C., Leng, W., Zhang, X., 2022. Laboratory evaluation of different geosynthetics for water drainage. Geosynth. Int. 29 (3), 254–269. https://doi.org/10.1680/jgein.21.00005.

Han, J., 2015. Principles and Practice of Ground Improvement. John Wiley & Sons.

Holtz, R.D., Christopher, B.R., Berg, R.R., 1998. Geosynthetic Design and Construction Guidelines.

Huang, M., Lin, C., Pokharel, S.K., Tura, A., Mukhopadhyaya, P., 2021. Model tests of freeze-thaw behavior of geocell-reinforced soils. Geotext. Geomembranes 49 (3), 669–687. https://doi.org/10.1016/j.geotexmem.2020.12.003.

Irrigation Association Water Management Committee (IA), 2005. Landscape Irrigation Scheduling and Water Management.

Jarjour, M., Meguid, M.A., 2024. Water retention characterization of non-woven geotextiles: an application for wicking materials. E3S Web Conf. 569, 12003. https://doi.org/10.1051/e3sconf/202456912003.

Khoury, C.N., Miller, G.A., Hatami, K., 2011. Unsaturated soil–geotextile interface behavior. Geotext. Geomembranes 29 (1), 17–28. https://doi.org/10.1016/j.geotexmem.2010.06.009.

Lin, C., Zhang, X., 2018. Laboratory drainage performance of a new geotextile with wicking fabric. J. Mater. Civ. Eng. 30 (11), 04018293. https://doi.org/10.1061/(ASCE)MT.1943-5533.0002476.

Lin, C., Zhang, X., 2020. Comparisons of geotextile-water characteristic curves for wicking and non-wicking geotextiles. GeoCongress 2020, 629–636. https://doi.org/10.1061/9780784482797.061.

Lin, C., Zhang, X., Galinmoghadam, J., Guo, Y., 2022. Working mechanism of a new wicking geotextile in roadway applications: a numerical study. Geotext. Geomembranes 50 (2), 323–336. https://doi.org/10.1016/j.geotexmem.2021.11.009.

Liu, J., Lin, C., Liu, M., Bhat, S., 2024. Repeated load triaxial tests of WickGrid™ stabilized base materials. E3S Web Conf. 569, 21006. https://doi.org/10.1051/e3sconf/202456921006.

Liu, H., Han, J., Al-Naddaf, M., Parsons, R.L., Kakrasul, J.I., 2022. Field monitoring of wicking geotextile to reduce soil moisture under a concrete pavement subjected to precipitations and temperature variations. Geotext. Geomembranes 50 (5), 1004–1019. https://doi.org/10.1016/j.geotexmem.2022.07.001.

Liu, M., Liu, J., Bhat, S., Gupta, R., Lin, C., 2025. Laboratory Evaluation of Water Removal Capability of Wicking Nonwoven Geotextiles [Unpublished manuscript].

Lim, S.-M., Indraratna, B., Heitor, A., Yao, K., Jin, D., Albadri, W.M., Liu, X., 2022. Influence of matric suction on resilient modulus and CBR of compacted Ballina clay. Constr. Build. Mater. 359, 129482.

Navas, A., Alberto, F., Machín, J., Galán, A., 1990. Design and operation of a rainfall simulator for field studies of runoff and soil erosion. Soil Technol. 3 (4), 385–397. https://doi.org/10.1016/0933-3630(90)90019-Y.

Pokharel, S.K., Han, J., Leshchinsky, D., Parsons, R.L., Halahmi, I., 2010. Investigation of factors influencing behavior of single geocell-reinforced bases under static loading. Geotext. Geomembranes 28 (6), 570–578. https://doi.org/10.1016/j.geotexmem.2010.06.002.

Rajagopal, K., Chandramouli, S., Parayil, A., Iniyan, K., 2014. Studies on geosynthetic-reinforced road pavement structures. Int. J. Geotech. Eng. 8 (3), 287–298. https://doi.org/10.1179/1939787914Y.0000000042.

Rollin, A., Lombard, G., 1988. Mechanisms affecting long-term filtration behavior of geotextiles. Geotext. Geomembranes 7 (1–2), 119–145.

Sheridan, G.J., Noske, P.J., Lane, P.N.J., Sherwin, C.B., 2008. Using rainfall simulation and site measurements to predict annual interrill erodibility and phosphorus generation rates from unsealed forest roads: validation against in-situ erosion measurements. Catena 73 (1), 49–62. https://doi.org/10.1016/j.catena.2007.08.006.

Sicha, G., Zornberg, J., 2023. Quantification of Suction-Driven Flow of Enhanced Lateral Drainage Geotextiles.

Sosa-Pérez, G., MacDonald, L.H., 2017. Effects of closed roads, traffic, and road decommissioning on infiltration and sediment production: a comparative study using rainfall simulations. Catena 159, 93–105. https://doi.org/10.1016/j.catena.2017.08.004.

Wang, F., Han, J., Zhang, X., Guo, J., 2017. Laboratory tests to evaluate effectiveness of wicking geotextile in soil moisture reduction. Geotext. Geomembranes 45 (1), 8–13. https://doi.org/10.1016/j.geotexmem.2016.08.002.

Zhang, X., Presler, W., Li, L., Jones, D., Odgers, B., 2014. Use of wicking fabric to help prevent frost boils in Alaskan pavements. J. Mater. Civ. Eng. 26 (4), 728–740. https://doi.org/10.1061/(ASCE)MT.1943-5533.0000828.

Zaman, M.W., Han, J., Kabir, M.U., Parsons, R.L., 2024. Laboratory evaluation of wicking geotextile for moisture reduction in silty sands at different fines contents. Geotext. Geomembranes 52 (6), 1180–1190. https://doi.org/10.1016/j.geotexmem.2024.08.001.

Zaman, M.W., Han, J., Zhang, X., 2022. Evaluating wettability of geotextiles with contact angles. Geotext. Geomembranes 50 (4), 825–833. https://doi.org/10.1016/j.geotexmem.2022.03.014.

Zemke, J., 2016. Runoff and soil erosion assessment on forest roads using a small scale rainfall simulator. Hydrology 3 (3), 25. https://doi.org/10.3390/hydrology3030025.